

# P-Bifurcations in Stochastic Flutter Model Under Common Gust Perturbations

Sunia Tanweer<sup>1,2\*</sup>

Firas A. Khasawneh<sup>2</sup>

1. Dept. of Mechanical Engineering, Michigan State University

2. Dept. of Computational Mathematics, Science and Engineering, Michigan State University

## Abstract

Aeroelastic flutter represents a critical nonlinear instability in flight dynamics, where the coupling between structural elasticity and unsteady aerodynamics leads to self-excited oscillations. In deterministic settings, the onset of flutter is typically characterized by bifurcations of invariant sets such as equilibria or limit cycles. However, real flight conditions are inherently stochastic due to atmospheric turbulence, rendering trajectory-based attractors insufficient for describing long-time behavior and motivating a probabilistic viewpoint. The stochastic nature of turbulence modifies these transitions, often generating high-dimensional stationary distributions which are difficult to visualize. In this work, we use a topological framework to detect and characterize such stochastic bifurcations in a two-degree-of-freedom aerofoil model with nonlinear stiffness. Reconstructing the full phase-space kernel density estimate (KDE) and constructing homological bifurcation plots reveal high-dimensional toroidal structures in the stationary probability density that are otherwise difficult to detect from two-dimensional projections. Further, we perform a comparative analysis of flutter under the influence of three classes of gust models: sinusoidal white Gaussian noise, the Dryden turbulence model, and the Von Karman turbulence model. Our analysis bypasses the predominantly used visual inspection in stochastic bifurcation studies, enabling systematic and automated exploration of stochastic flutter across large parameter ranges.

## 1 Introduction

Aeroelastic systems manifest very complex phenomena due to interactions between aerodynamic forces and structural elements of flexible bodies. One of the most important phenomenon within these systems is flutter—a self-excited oscillation that may lead to structural failure due to large amplitude oscillations [1, 2]. Among such nonlinear behaviors, an important type known as stall flutter occurs in aerofoils when flow separates at high angles of attack and creates an eminent threat to aircraft stability [3, 4].

When the aerofoil is subject to random wind gust excitation or when uncertainties in the system parameters are present, stochastic analysis becomes necessary for ensuring aviation safety through instability prediction and mitigation. For example, the interaction between the aerofoil and unsteady fluid flows can lead to complex phenomena like intermittency that contribute to stall and flutter [5]. As the angle of attack increases, the airflow may separate from the surface, causing oscillations that can be exacerbated by stochastic influences. The resulting flow patterns can significantly alter the stability of the aerofoil, making stochastic analysis crucial for predicting and mitigating flutter risks [6–8]. One tool that can be used to study shifts in the response of a stochastic systems is stochastic bifurcation analysis.

Stochastic bifurcation [9, 10] is a critical concept in understanding the dynamics of aerofoil stall and flutter [5], particularly under the influence of random disturbances. In the context of aerofoils, stochastic bifurcation helps identify the critical points where small changes in parameters can lead to large-scale

\*tanweer1@msu.edu

shifts in behavior, such as transitioning from stable to unstable conditions [11]. This analysis is essential for understanding limit cycle oscillations (LCOs) that are commonly experienced during stall flutter, as they indicate the onset of instability [12].

The interrelation between stochastic bifurcation and stall flutter remains a topic of active research. Recent studies have focused on the stochastic analysis of flutter in multi-stable aerofoils, where the role of random disturbances is central to understanding oscillatory behavior during stall conditions [13–15]. These investigations demonstrate that statistical methods can characterize bifurcation behavior and predict flutter conditions, which is vital for the design of safer and more efficient aerofoils [14]. However, most existing approaches rely heavily on visual inspection of low-dimensional phase portraits, time series, or probability density plots, which limits the number of state variables and parameters that can be examined simultaneously, such as here [5]. Such low-dimensional projections can obscure essential features of the underlying dynamics in inherently high-dimensional aeroelastic systems. Moreover, the reliance on manual inspection precludes rigorous, automated analysis over large parameter ranges, making comprehensive uncertainty quantification and comparative studies difficult. In addition, prior stochastic flutter studies predominantly consider simplified sinusoidal or narrow-band excitation models, whereas modern aviation applications commonly employ physically grounded turbulence models such as the Dryden and Von Karman spectra [16]. In contrast, the present work provides a topology-based, automated framework for detecting stochastic flutter bifurcations directly from high-dimensional stationary distributions, and systematically compares bifurcation behavior across sinusoidal, Dryden, and Von Karman gust models.

This paper discusses the bifurcation behavior of aeroelastic systems with conditions representative of stall flutter. Our analysis—conducted on a multi-stable aerofoil dynamics—investigates the influence of various types of stochastic parametric excitation on flutter behavior of the aerofoil and how bifurcations manifest under a stochastic framework. The full state of the system spans a four-dimensional phase space in pitch, plunge, and their velocities, making direct visualization of its evolution and attractor geometry infeasible. We use Topological data analysis (TDA) [17] to quantify these structures by characterizing the shape of the underlying probability density through its homological features such as connected components, loops, and voids to detect and classify bifurcations without relying on visual inspection. Critical bifurcation points due to the high-dimensionality of the model are computed using homological bifurcation plots [18]. This plot identifies the critical points where small changes in parameters can lead to a shift from monostability to limit-cycle oscillations (LCOs)—which are indicative of instability.

## 2 Mathematical Background

### 2.1 Stochastic Attractors and Invariant Distribution

For deterministic dynamical systems, long-time behavior is characterized by invariant sets such as fixed points, limit cycles, or strange attractors. In contrast, stochastic dynamical systems do not admit trajectory-wise invariant sets due to continual random perturbations. Instead, their asymptotic behavior is described either in terms of random attractors or, equivalently under suitable conditions, invariant probability measures.

In this work, we adopt the framework of pullback attractors for random dynamical systems. A pullback attractor is a random, time-dependent set that attracts all initial conditions when trajectories are pulled back to the distant past and evolved forward under a fixed realization of the noise [19, 20]. When the stochastic system is ergodic, the pullback attractor induces a unique stationary (invariant) probability measure, which describes the long-time distribution of system states independently of initial conditions.

Rather than attempting to compute the pullback attractor itself, we will focus on the topology of the associated stationary probability distribution. Specifically, we reconstruct the invariant measure using long-time Monte Carlo sampling and kernel density estimation, and analyze the topology of its high-probability

regions via superlevel-set persistent homology. Topological changes in this stationary distribution provide a robust and quantitative signature of phenomenological (P-)bifurcations in the stochastic system.

## 2.2 Aerofoil Model

A two-degree-of-freedom (2-DOF) aerofoil system, adopted from Venkatramani et al. [5], has been used to model the coupled pitch and plunge motions responsible for stall flutter. The aerofoil is free to oscillate vertically (plunge,  $\epsilon$ ) and rotationally (pitch,  $\alpha$ ) about its elastic axis. The governing equations of motion, expressed in nondimensional form, are written as

$$\epsilon'' + x_\alpha \alpha'' + 2\zeta_\epsilon \frac{\omega}{U} \epsilon' + \left(\frac{\omega}{U}\right)^2 (\epsilon + \beta_\epsilon \epsilon^3) = -\frac{1}{\pi \mu} C_L(\tau), \quad (1)$$

$$\frac{x_\alpha}{r_\alpha^2} \epsilon'' + \alpha'' + 2\zeta_\alpha \frac{1}{U} \alpha' + \frac{1}{U^2} (\alpha + \beta_\alpha \alpha^3) = \frac{2}{\pi \mu r_\alpha^2} C_M(\tau). \quad (2)$$

The cubic stiffness terms  $\beta_\epsilon, \beta_\alpha$  capture geometric nonlinearities responsible for LCOs. Figure 1 shows a schematic of the model, and Table 1 shows the values used for all of the properties used in the simulations.

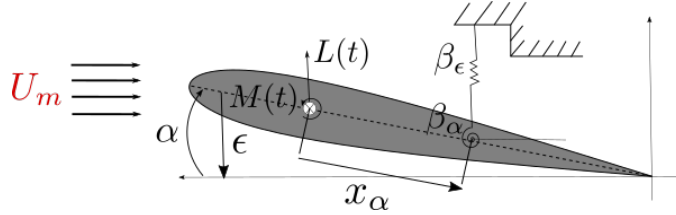


Figure 1: 2-DOF aerofoil model with pitch and plunge motion.

Parameter	Symbol	Value
Elastic-axis offset (from mid-chord)	$x_\alpha$	0.29
Radius of gyration (about elastic axis)	$r_\alpha$	0.707
Mass ratio	$\mu$	660.0
Aerodynamic center offset	$a_h$	-0.5
Plunge cubic stiffness coefficient	$\beta_\epsilon$	3.0
Pitch cubic stiffness coefficient	$\beta_\alpha$	0
Pitch damping ratio	$\zeta_\alpha$	0.03
Plunge damping ratio	$\zeta_\epsilon$	0.05
Frequency ratio (plunge/pitch)	$\omega$	0.999

Table 1: Properties of the 2-DOF aerofoil model used for all simulations.

The unsteady lift  $C_L$  and moment  $C_M$  coefficients are computed using Theodorsen-type approximations with a Wagner function, which accounts for wake-induced memory effects according to

$$\phi(\tau) = 1 - 0.165e^{-0.0455\tau} - 0.335e^{-0.3\tau}, \quad (3)$$

so that

$$C_L(\tau) = 2\pi[\alpha(0) + \epsilon'(0) + (0.5 - a_h)\alpha'(0)]\phi(\tau) + 2\pi \int_0^\tau \phi(\tau - \sigma) [\alpha'(\sigma) + \epsilon''(\sigma) + (0.5 - a_h)\alpha''(\sigma)] d\sigma + \pi(\epsilon'' - a_h\alpha'' + \alpha'), \quad (4)$$

$$C_M(\tau) = \pi(0.5 + a_h)[\alpha(0) + \epsilon'(0) + (0.5 - a_h)\alpha'(0)]\phi(\tau) + \pi(0.5 + a_h) \int_0^\tau \phi(\tau - \sigma) [\alpha'(\sigma) + \epsilon''(\sigma) + (0.5 - a_h)\alpha''(\sigma)] d\sigma. \quad (5)$$

The convolution structure implies that current aerodynamic forces depend on the past history of aerofoil motion, introducing intrinsic phase delay and enabling quasiperiodic responses.

### 2.3 Stochastic Flow-Speed Excitation Models

To examine the influence of turbulence spectra on flutter dynamics, the incoming flow velocity is modeled as

$$U(\tau) = U_m + \sigma\Delta U(\tau), \quad (6)$$

where  $U_m$  is the mean flow speed and  $\Delta U(\tau)$  represents stochastic fluctuations. In addition to the sinusoidal perturbation model considered in the literature [5], we study Dryden and Von Karman turbulence models. These three excitation models—shown in Fig. 2—are described below.

#### (a) Sinusoidal perturbation:

$$\Delta U = U_m \sin(\omega_r \tau) \quad (7)$$

where  $\omega_r$  is a fluctuating frequency modeled as  $\omega_r = \omega_1 + \kappa R(\tau)$ , with  $R(\tau)$  being a random variable.

**(b) Dryden turbulence model [16]:** The velocity  $\Delta U = u(t)$  is generated by the first-order shaping filter

$$\dot{u}(t) = -\frac{U_m}{L_u}u(t) + \sqrt{\frac{2\sigma_u^2 U_m}{L_u}}\eta(t), \quad (8)$$

where  $L_u$  is the turbulence length scale and  $\sigma_u^2$  its variance. The resulting spectrum decays as  $S(f) \propto (1 + L_u^2 f^2)^{-1}$ , producing smoothly correlated fluctuations.

**(c) Von Karman turbulence model [16]:** A second-order shaping filter approximates the Von Karman spectrum,

$$\ddot{u}(t) + 2\zeta_u \omega_u \dot{u}(t) + \omega_u^2 u(t) = \sqrt{2\sigma_u^2 \omega_u^3} \eta(t), \quad (9)$$

with damping ratio  $\zeta_u$  and break frequency  $\omega_u = U_m/L_u$ . Compared with the Dryden model, it yields a steeper high-frequency roll-off and more physically realistic coherence of turbulence eddies.

## 3 Methods

We will use homological bifurcation analysis to detect phenomenological bifurcations in stochastic systems [18] and apply it to the four-dimensional KDEs estimated from the state-space response using 100 monte carlo simulations per mean speed  $U_m \in [2, 10]$ . The following sections describe the homological bifurcation analysis framework, while the bandwidth estimation used for the KDEs is described in Appendix B.

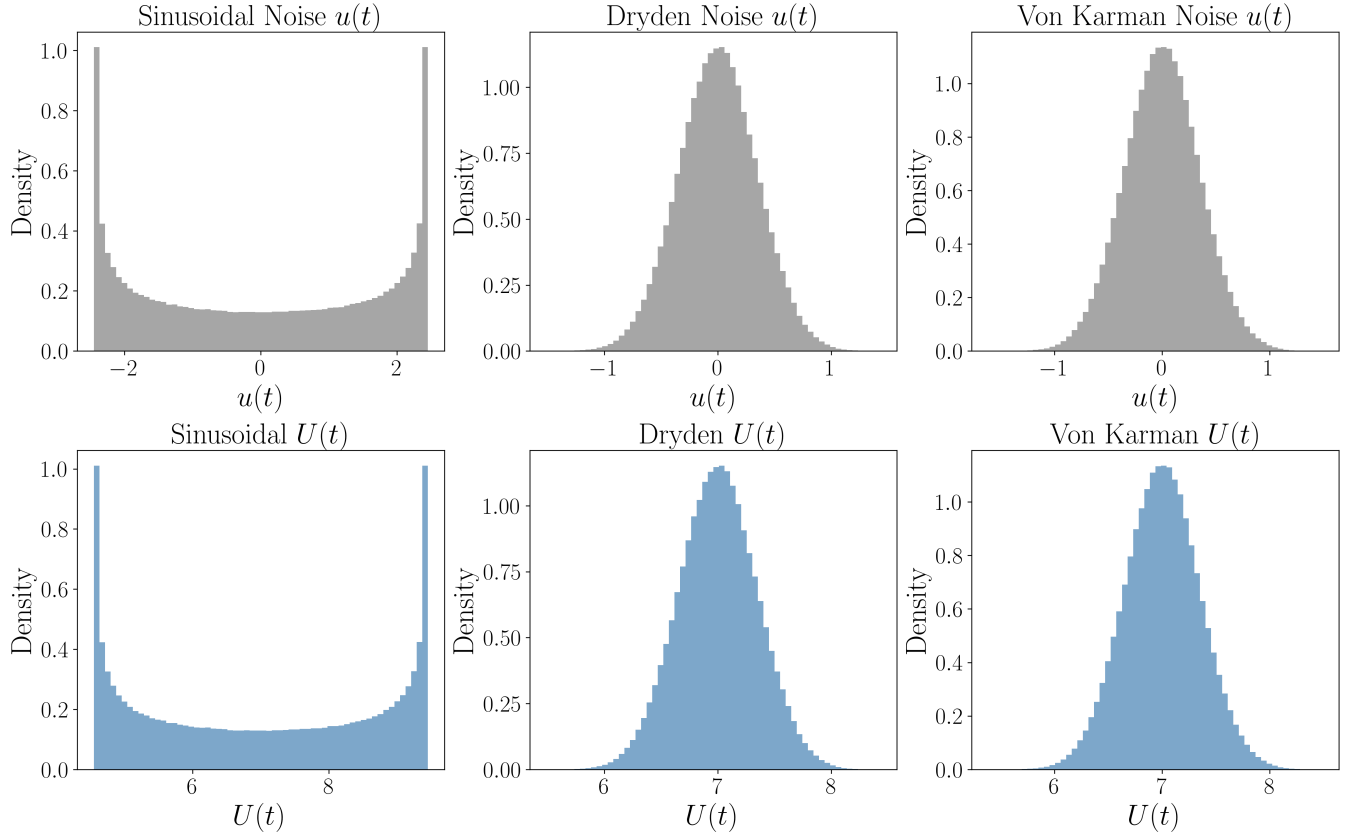


Figure 2: Stochastic gust excitation models considered in this study: sinusoidal, Dryden, and Von Karman. The top row shows the probability distributions of the stochastic velocity fluctuations  $u(t)$  generated by each excitation model, while the bottom row shows the corresponding distributions of the resulting flow speed  $U(t)$  used in the aeroelastic simulations.

### 3.1 Superlevel persistence of the probability density function

Given a unit-normalized stationary KDE  $p(\mathbf{x})$  of the aerofoil state vector  $\mathbf{x} = [\alpha, \epsilon, \dot{\alpha}, \dot{\epsilon}]$ , we construct a *superlevel filtration* of cubical complexes (see [18] or Appendix A for more details on this)

$$K_{L_1} \subseteq K_{L_2} \subseteq \cdots \subseteq K_{L_N}, \quad \text{where } K_L = p^{-1}([L, \infty)).$$

Each cubical complex  $K_L$  represents the subset of phase space where the KDE exceeds a probability threshold  $L$ . As  $L$  decreases from its maximum value to zero, high-probability regions merge and new topological features (connected components, loops, or voids) appear and disappear. Persistent homology quantifies these topological features by tracking the birth and death of homology classes as a function of  $L$ .

For the aeroelastic model, we compute persistence over  $H_0$ ,  $H_1$ , and  $H_2$  homology groups corresponding to connected components, limit-cycle loops, and voids, respectively.

### 3.2 Homological bifurcation plots

A family of KDEs  $\{p_i(\mathbf{x})\}$  is generated by varying the bifurcation parameter—here, the mean flow speed  $U_m$ . For each  $p_i(\mathbf{x})$ , the persistence computation yields a vector of Betti numbers

$$\boldsymbol{\beta}_i = [\beta_i(L_1), \beta_i(L_2), \dots, \beta_i(L_N)],$$

where  $i$  values of 0, 1, and 2 give the vectors  $\boldsymbol{\beta}_0$ ,  $\boldsymbol{\beta}_1$ , and  $\boldsymbol{\beta}_2$ , respectively. These Betti vectors are then stacked over the range of  $U_m$  values to form a two-dimensional map showing how each homology group evolves across both the filtration parameter and the bifurcation parameter.

The resulting heatmap—referred to as a *homological bifurcation plot* [18]—provides a quantitative visualization of changes in the topology of the KDE. Abrupt transitions in the rank of a homology group  $\beta_p$  indicate a qualitative shift in the system’s probabilistic structure and thus mark a P-bifurcation. See Fig. 3 for a schematic of the method.

## 4 Results and Discussion

The stochastic equations were integrated for a range of mean flow speeds  $U_m$  for each turbulence model and the long-term system response

$$\mathbf{x}(t) = (\epsilon, \alpha, \dot{\epsilon}, \dot{\alpha})$$

was sampled to reconstruct the four-dimensional state-space probability density function using kernel density estimation. The density was normalized to unit total probability, and its topological evolution was examined using homological bifurcation plots over the normalized filtration parameter  $\rho \in [0, 1]$ .

We first examine the direct dynamical response of the aeroelastic system in the time domain and in low-dimensional phase-space projections in Section 4.1 followed by the topological analysis in Section 4.2.

### 4.1 Time–Domain and Phase–Space Response Across Flow Speeds

Figures 4 and 5 summarize representative time histories and phase portraits for three mean-flow speeds—a subcritical regime ( $U_m = 2.5$ ), a near-critical regime ( $U_m = 4.5$ ), and a clearly supercritical regime ( $U_m = 10.0$ ).

At low flow speeds ( $U_m = 2.5$ ), all three models exhibit strongly damped transient responses. The pitch and plunge displacements, along with their velocities, decay to zero. Dryden and Von Karman excitations introduce small stochastic perturbations, but these remain well within the linear decay envelope too.

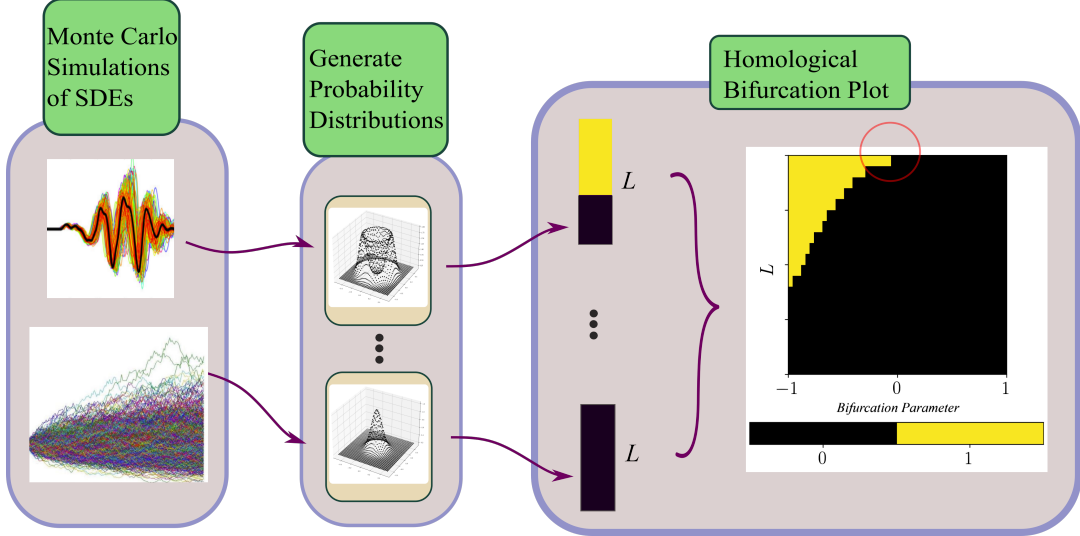


Figure 3: Schematic overview of the homological bifurcation analysis framework. Monte Carlo simulations generate ensembles of trajectories which are used to estimate the distribution. Superlevel filtration of cubical complexes is computed for each KDE, and the resulting Betti vectors yield the homological bifurcation plot,

The corresponding phase-space trajectories collapse to a single point, reflecting a unimodal stationary density. As the flow speed approaches the instability threshold ( $U_m = 4.5$ ), differences among the three models begin to emerge. The sinusoidal excitation still produces a decaying response, with no growth in amplitude. In contrast, both Dryden and Von Karman turbulence inject sufficient correlated energy to generate intermittent bursts of oscillation. These appear as modulated time-series envelopes and as broadened, partially closed loops in the  $(\varepsilon, \alpha)$ ,  $(\varepsilon, \dot{\alpha})$ , and  $(\alpha, \dot{\alpha})$  projections—although the system remains nominally stable due to the low amplitude of these. For supercritical flow speeds ( $U_m = 10.0$ ), all three excitation models lead to sustained large-amplitude oscillations in pitch and plunge.

Overall, the time-domain and phase-space responses confirm that turbulence models with temporal correlation (Dryden and Von Karman) accelerate the onset of flutter-like oscillatory behavior and yield richer oscillatory structure above the critical flow speed, a trend that we quantitatively capture using the topological signatures presented in the following sections.

## 4.2 Homological Bifurcation Plots

Figure 6 shows the homological bifurcation plots for the three turbulence models across the first three homology dimensions. The horizontal axis corresponds to the mean flow speed  $U_m$ , and the vertical axis corresponds to the superlevel parameter  $\varepsilon$  of the cubical complex filtration. Each color indicates the Betti number  $\beta_k$  detected at that resolution, allowing us to identify when new connected components ( $H_0$ ), loops ( $H_1$ ), or voids ( $H_2$ ) emerge in the stationary probability density.

**Connected Components ( $H_0$ ):** For sinusoidal excitation, the density remains unimodal until approximately  $U_m \approx 5.5$  m/s, at which point the homological signature transitions from  $\beta_0 = 1$  to  $\beta_0 = 2$ . This transition is sharp and confined to a relatively narrow band of  $\varepsilon$ , consistent with the delayed instability onset seen in the time-domain dynamics. In contrast, both Dryden and Von Karman turbulence exhibit earlier and less abrupt transitions in  $H_0$ . Under correlated turbulence, the density splits into multiple component as early as  $U_m \approx 5$  m/s, and this multi-component structure persists over a broader range of

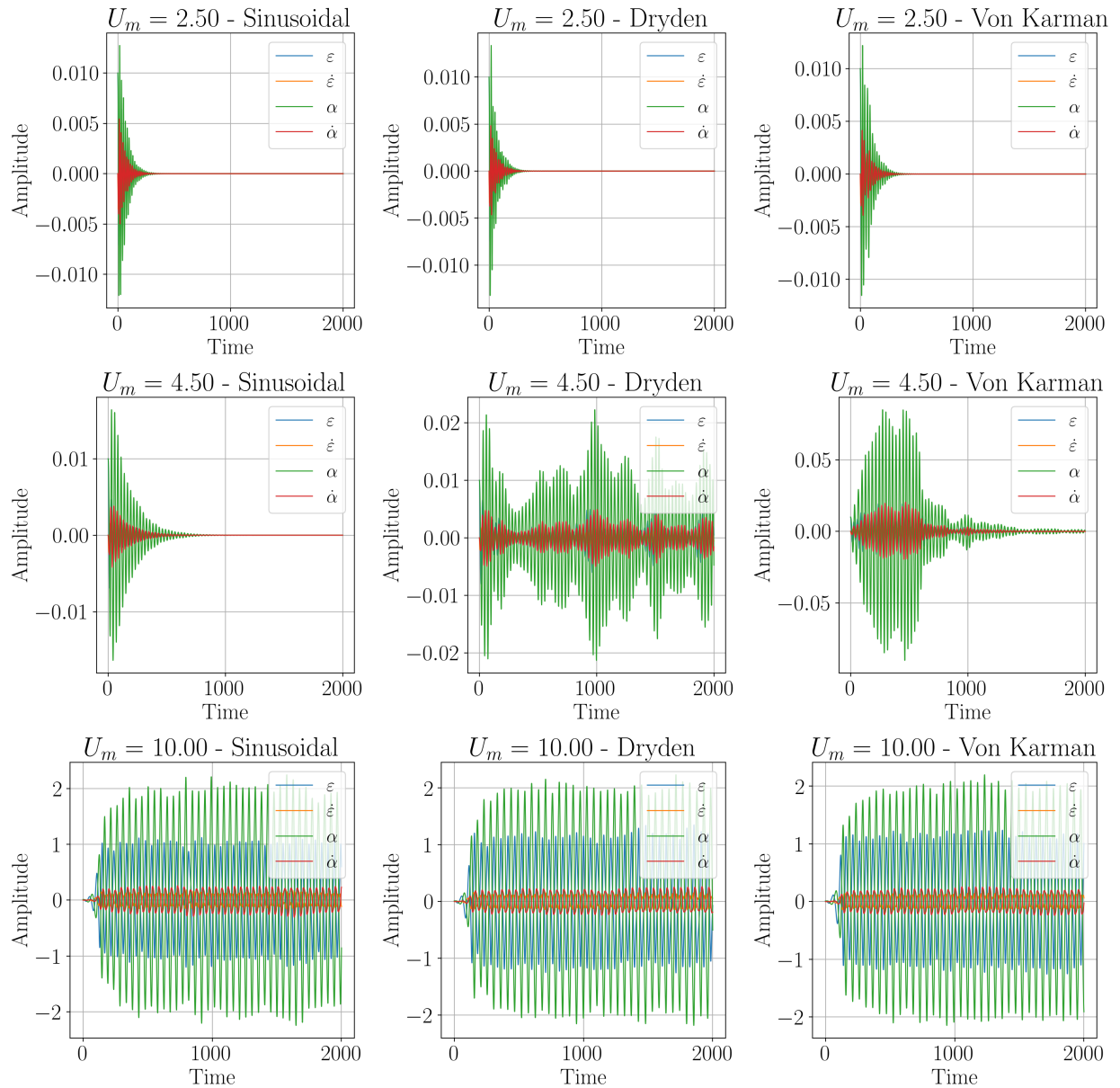


Figure 4: Representative time-series of pitch  $\alpha(t)$  and plunge  $\epsilon(t)$  with their velocities, at subcritical, near-critical, and supercritical flow speeds for the sinusoidal, Dryden, and Von Karman excitation models.

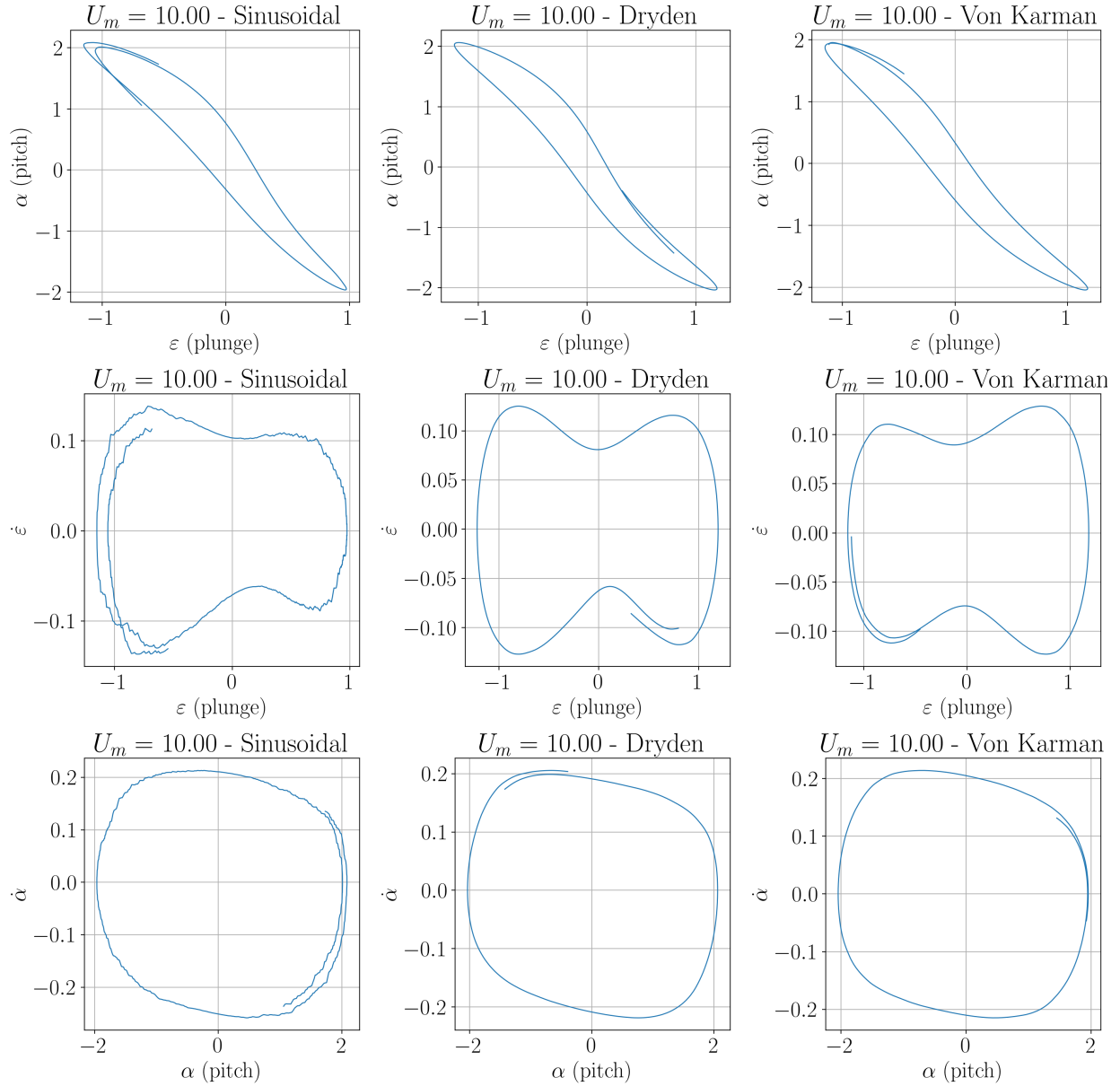


Figure 5: Representative phase-space projections  $(\alpha, \varepsilon)$ ,  $(\varepsilon, \dot{\omega})$  and  $(\alpha, \dot{\alpha})$  showing limit cycles for the three noise models at a speed of 10 m/s. The limit cycles are very narrow in  $(\alpha, \varepsilon)$  space, but wider in the other two.

superlevel thresholds. This earlier appearance of  $\beta_0 = 2$  (and occasionally  $\beta_0 = 3, 4$ ) reflects the fact that colored stochastic fluctuations can intermittently push the system toward flutter-like oscillations before the deterministic threshold.

**Limit-Cycle Loops ( $H_1$ ):** The transition in the first homology group occurs around the same speed as  $H_0$  transitions. For sinusoidal excitation, persistent  $H_1$  loops emerge around  $U_m \approx 5.5$  m/s, matching the onset of clean, periodic limit cycles in the phase-space trajectories. Dryden and Von Karman turbulence again produce earlier transitions with  $\beta_1 > 0$  appearing as early as  $U_m \approx 4.75$  m/s. In these models, the  $H_1$  “bifurcation tongue” slopes downward with increasing  $U_m$ , indicating that while loops are born early, they persist mainly at intermediate probability levels.

**Toroidal Cavities ( $H_2$ ):** Although  $H_2$  features are weaker and more sporadic, all three models show some regions with  $\beta_2 = 1$ , primarily beyond  $U_m \approx 5$  m/s. These correspond to superlevel sets forming toroidal pockets in the estimated density, which occur when the stationary distribution develops a fully three-dimensional donut-like geometry in  $(\alpha, \dot{\alpha}, \varepsilon, \dot{\varepsilon})$ -space. The  $H_2$  features appear sparsely for two reasons. First, the loops in this phase space are extremely thin, so the corresponding high-probability shell is narrow and susceptible to getting numerically smoothed out in the KDE. Second, the presence of noise (especially correlated noise) smears the torus, flattening it and reducing the persistence of the central void.

## 5 Conclusion

This work compares the effect of different noise models on appearance of stochastic bifurcations in a two-degree-of-freedom aeroelastic system subject to three forms of parametric excitation—sinusoidal fluctuations, Dryden turbulence, and Von Karman turbulence. By constructing full-phase-space probability densities and analyzing their topology, we identified transitions in  $\beta_0$ ,  $\beta_1$ , and  $\beta_2$  that signal the appearance of multi-modal distributions, limit-cycle loops, and toroidal voids respectively. The homological bifurcation plots revealed that each excitation model induces a distinct bifurcation pattern. Sinusoidal forcing produced the latest transitions while both Dryden and Von Karman turbulence generated earlier transitions. The correlated nature of these turbulence models accelerates the onset of flutter-like behavior. Although the second homology  $\beta_2$  appeared less frequently, isolated pockets of non-zero  $\beta_2$  were detected for all three models at flow speeds beyond approximately  $U_m \approx 5$  m/s. These correspond to thin toroidal cavities in the probability density, arising when the limit cycle acquires a three-dimensional shell structure in the full phase space. Their sparse appearance is attributed to the narrowness of these structures and the smoothing inherent in kernel density estimation. Nevertheless, their presence confirms that the stochastic aeroelastic response can transiently occupy a toroidal manifold, particularly under correlated turbulence.

Although our analysis used an example stochastic flutter model, the approach we present can be applied to different models and with different gust conditions. It can further be automated to conduct large-scale parameter studies on flutter phenomenon.

## 6 Acknowledgements

This material is based upon work supported by the Air Force Office of Scientific Research under award number FA9550-26-1-0011, and by the NSF Frontera Computational Science Fellowship awarded to ST for 2025-2026.

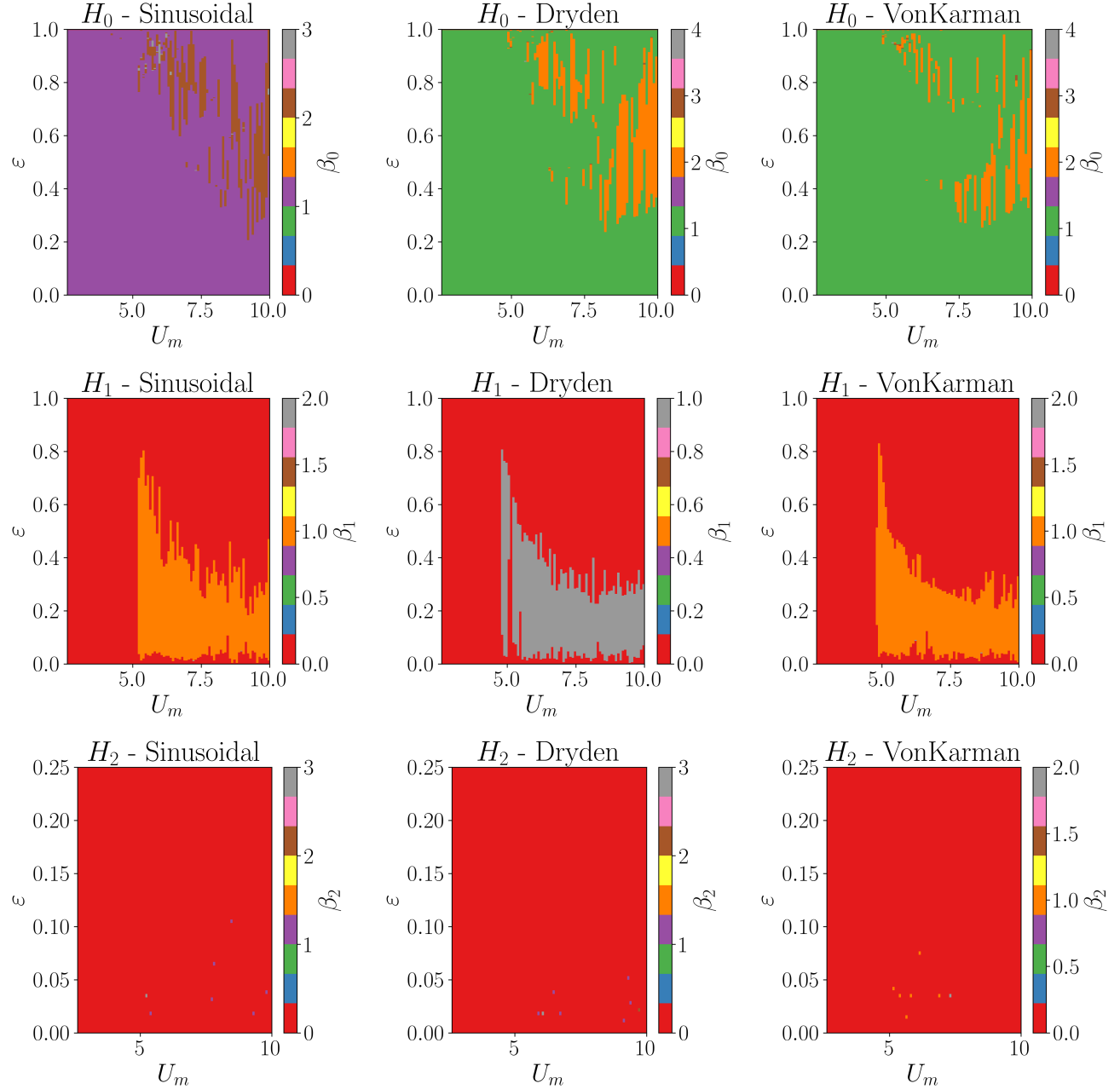


Figure 6: Homological bifurcation plots for the sinusoidal, Dryden, and Von Karman models. The x-axis is the mean flow speed  $U_m$ , the y-axis is the normalized filtration level, and color represents the number of connected components  $\beta_p$ . Note: The scale for  $H_2$  is intentionally cropped for as the  $\beta_2 > 0$  values appear for small filtrations only.

## References

- [1] Marco Berci. "On Aerodynamic Models for Flutter Analysis: A Systematic Overview and Comparative Assessment". In: *Applied Mechanics* 2.3 (July 2021), 516–541. ISSN: 2673-3161. DOI: [10.3390/applmech2030029](https://doi.org/10.3390/applmech2030029). URL: <http://dx.doi.org/10.3390/applmech2030029>.
- [2] K. D. Jones and M. F. Platzer. "Time-domain analysis of low-speed airfoil flutter". In: *AIAA Journal* 34.5 (May 1996), 1027–1033. ISSN: 1533-385X. DOI: [10.2514/3.13183](https://doi.org/10.2514/3.13183). URL: <http://dx.doi.org/10.2514/3.13183>.
- [3] Shantanu S. Bhat and Raghuraman N. Govardhan. "Stall flutter of NACA 0012 airfoil at low Reynolds numbers". In: *Journal of Fluids and Structures* 41 (Aug. 2013), 166–174. ISSN: 0889-9746. DOI: [10.1016/j.jfluidstructs.2013.04.001](https://doi.org/10.1016/j.jfluidstructs.2013.04.001). URL: <http://dx.doi.org/10.1016/j.jfluidstructs.2013.04.001>.
- [4] Xintao Li, Yonghe Cui, Baoliang Li, and Mingwei Ge. "Mechanism of airfoil stall flutter: New insights from global linear stability analysis". In: *Physics of Fluids* 36.11 (Nov. 2024). ISSN: 1089-7666. DOI: [10.1063/5.0235196](https://doi.org/10.1063/5.0235196). URL: <http://dx.doi.org/10.1063/5.0235196>.
- [5] J. Venkatramani, Sunetra Sarkar, and Sayan Gupta. "Intermittency in pitch-plunge aeroelastic systems explained through stochastic bifurcations". In: *Nonlinear Dynamics* 92.3 (Feb. 2018), 1225–1241. ISSN: 1573-269X. DOI: [10.1007/s11071-018-4121-5](https://doi.org/10.1007/s11071-018-4121-5). URL: <http://dx.doi.org/10.1007/s11071-018-4121-5>.
- [6] Zhen Chen, Zhiwei Shi, Sinuo Chen, and Zhangyi Yao. "Stall flutter suppression of NACA 0012 airfoil based on steady blowing". In: *Journal of Fluids and Structures* 109 (Feb. 2022), p. 103472. ISSN: 0889-9746. DOI: [10.1016/j.jfluidstructs.2021.103472](https://doi.org/10.1016/j.jfluidstructs.2021.103472). URL: <http://dx.doi.org/10.1016/j.jfluidstructs.2021.103472>.
- [7] X. Y. Huang. "Active control of aerofoil flutter". In: *AIAA Journal* 25.8 (Aug. 1987), 1126–1132. ISSN: 1533-385X. DOI: [10.2514/3.9753](https://doi.org/10.2514/3.9753). URL: <http://dx.doi.org/10.2514/3.9753>.
- [8] You Wu, Yuting Dai, and Chao Yang. "Time-Delayed Active Control of Stall Flutter for an Airfoil via Camber Morphing". In: *AIAA Journal* 60.10 (Oct. 2022), 5723–5734. ISSN: 1533-385X. DOI: [10.2514/1.j061947](https://doi.org/10.2514/1.j061947). URL: <http://dx.doi.org/10.2514/1.J061947>.
- [9] N. Sri Namachchivaya. "Stochastic bifurcation". In: *Applied Mathematics and Computation* 38.2 (July 1990), 101–159. ISSN: 0096-3003. DOI: [10.1016/0096-3003\(90\)90051-4](https://doi.org/10.1016/0096-3003(90)90051-4). URL: [http://dx.doi.org/10.1016/0096-3003\(90\)90051-4](http://dx.doi.org/10.1016/0096-3003(90)90051-4).
- [10] Richard F. Bass and Krzysztof Burdzy. "Stochastic Bifurcation Models". In: *The Annals of Probability* 27.1 (Jan. 1999). ISSN: 0091-1798. DOI: [10.1214/aop/1022677254](https://doi.org/10.1214/aop/1022677254). URL: <http://dx.doi.org/10.1214/aop/1022677254>.
- [11] Rajagopal V Bethi, Sai Vishal Reddy Gali, and J Venkatramani. "Identifying route to stall flutter through stochastic bifurcation analysis". In: *MATEC Web of Conferences* 211 (2018). Ed. by N. Maia and Z. Dimitrovová, p. 02011. ISSN: 2261-236X. DOI: [10.1051/matecconf/201821102011](https://doi.org/10.1051/matecconf/201821102011). URL: <http://dx.doi.org/10.1051/matecconf/201821102011>.
- [12] Dimitrios Ketseas. "Stochastic Response of an Airfoil and Its Effects on LCO's Behavior Under Stall Flutter Regime". In: *International Journal of Mathematics, Statistics, and Computer Science* 2 (Jan. 2024), 168–172. ISSN: 2704-1077. DOI: [10.59543/ijmcs.v2i.8663](https://doi.org/10.59543/ijmcs.v2i.8663). URL: <http://dx.doi.org/10.59543/ijmcs.v2i.8663>.
- [13] Saied Irani, Saeid Sazesh, and Vahid Reza Molazadeh. "Flutter analysis of a nonlinear airfoil using stochastic approach". In: *Nonlinear Dynamics* 84.3 (Jan. 2016), 1735–1746. ISSN: 1573-269X. DOI: [10.1007/s11071-016-2601-z](https://doi.org/10.1007/s11071-016-2601-z). URL: <http://dx.doi.org/10.1007/s11071-016-2601-z>.

[14] Y. Hao and Z. Q. Wu. “Random Flutter of Multi-Stable Airfoils Excited Parametrically in Steady Flows”. In: *Journal of Mechanics* 35.3 (July 2018), 419–426. ISSN: 1811-8216. DOI: [10.1017/jmech.2018.19](https://doi.org/10.1017/jmech.2018.19). URL: <http://dx.doi.org/10.1017/jmech.2018.19>.

[15] Dheeraj Tripathi, R. Shreenivas, Chandan Bose, Sirshendu Mondal, and J. Venkatramani. “Experimental investigation on the synchronization characteristics of a pitch-plunge aeroelastic system exhibiting stall flutter”. In: *Chaos: An Interdisciplinary Journal of Nonlinear Science* 32.7 (July 2022). ISSN: 1089-7682. DOI: [10.1063/5.0096213](https://doi.org/10.1063/5.0096213). URL: <http://dx.doi.org/10.1063/5.0096213>.

[16] T. R. Beal. “Digital simulation of atmospheric turbulence for Dryden and von Karman models”. In: *Journal of Guidance, Control, and Dynamics* 16.1 (Jan. 1993), 132–138. ISSN: 1533-3884. DOI: [10.2514/3.11437](https://doi.org/10.2514/3.11437). URL: <http://dx.doi.org/10.2514/3.11437>.

[17] Frédéric Chazal and Bertrand Michel. “An Introduction to Topological Data Analysis: Fundamental and Practical Aspects for Data Scientists”. In: *Frontiers in Artificial Intelligence* 4 (Sept. 2021). ISSN: 2624-8212. DOI: [10.3389/frai.2021.667963](https://doi.org/10.3389/frai.2021.667963). URL: <http://dx.doi.org/10.3389/frai.2021.667963>.

[18] Sunia Tanweer, Firas A. Khasawneh, Elizabeth Munch, and Joshua R. Tempelman. “A topological framework for identifying phenomenological bifurcations in stochastic dynamical systems”. In: *Nonlinear Dynamics* 112.6 (Feb. 2024), 4687–4703. ISSN: 1573-269X. DOI: [10.1007/s11071-024-09289-1](https://doi.org/10.1007/s11071-024-09289-1). URL: <http://dx.doi.org/10.1007/s11071-024-09289-1>.

[19] Ludwig Arnold. *Random Dynamical Systems*. Springer Berlin Heidelberg, 1998. ISBN: 9783662128787. DOI: [10.1007/978-3-662-12878-7](https://doi.org/10.1007/978-3-662-12878-7). URL: <http://dx.doi.org/10.1007/978-3-662-12878-7>.

[20] Hans Crauel and Franco Flandoli. “Attractors for random dynamical systems”. In: *Probability Theory and Related Fields* 100.3 (Sept. 1994), 365–393. ISSN: 1432-2064. DOI: [10.1007/bf01193705](https://doi.org/10.1007/bf01193705). URL: <http://dx.doi.org/10.1007/BF01193705>.

[21] Sunia Tanweer and Firas A. Khasawneh. “Unsupervised Learning of Density Estimates with Topological Optimization”. In: (2025). DOI: [10.48550/ARXIV.2512.08895](https://doi.org/10.48550/ARXIV.2512.08895). URL: <https://arxiv.org/abs/2512.08895>.

## A Topological Data Analysis

### A.1 Homology and Betti Numbers

Homology provides a quantitative description of the topological structure of a space by identifying its connected components, loops, and voids. For a topological space  $X$ , the  $p$ -th homology group  $H_p(X)$  encodes  $p$ -dimensional holes, and its rank is called the *Betti number*:

$$\beta_p(X) = \dim H_p(X).$$

Intuitively,  $\beta_0$  counts connected components,  $\beta_1$  counts one-dimensional loops, and  $\beta_2$  counts enclosed cavities or toroidal voids.

When homology is computed across a sequence of spaces related by inclusion, we obtain a *filtration*:

$$H_p(X_{a_1}) \rightarrow H_p(X_{a_2}) \rightarrow \cdots \rightarrow H_p(X_{a_n}),$$

where  $a_i$  denotes the value of the filtration parameter. Persistent homology studies the appearance (birth) and disappearance (death) of topological features across this filtration.

### A.2 Cubical Complexes and Superlevel Persistence

In this study, the state-space kernel density estimate (KDE) is discretized into an  $m \times n \times k \times l$  array, forming a *cubical complex*  $K$ . Each cube  $s_{i,j,k,l}$  is assigned a scalar value equal to its probability density, giving a function  $f : K \rightarrow \mathbb{R}$ . For a threshold  $L$ , the corresponding *superlevelset* is defined as

$$K_L = f^{-1}([L, \infty)),$$

which collects all cubes with density greater than or equal to  $L$ . As  $L$  decreases from the peak of the PDF to zero, high-probability regions merge, loops form, and cavities appear or vanish, representing the geometric structure of the probability distribution.

This family of nested complexes

$$K_{L_1} \subseteq K_{L_2} \subseteq \cdots \subseteq K_{L_N}$$

defines a *superlevel filtration*. The homology of each  $K_L$  is computed to yield the Betti numbers  $\beta_p(L)$ , and their variation over  $L$  defines a *Betti curve*. In discretized settings, the collection of values

$$[\beta_p(L_0), \beta_p(L_1), \dots, \beta_p(L_N)]$$

is referred to as a *Betti vector*. In this context, the filtration parameter  $L$  corresponds directly to the normalized probability density of the aeroelastic system's stationary KDE. See Fig. 7 for an illustrative example.

### A.3 Persistent Homology and Bifurcation Analysis

By repeating the above computation across a range of bifurcation parameters—here, the mean flow speed  $U_m$ —one obtains a two-dimensional field of Betti numbers:

$$\beta_p(U_m, L),$$

which is visualized as a *homological bifurcation plot*. Color represents the magnitude of the Betti number, the  $x$ -axis corresponds to the bifurcation parameter  $U_m$ , and the  $y$ -axis corresponds to the filtration threshold  $L$ . Abrupt changes in  $\beta_0$ ,  $\beta_1$ , or  $\beta_2$  signify topological transitions in the system's invariant measure.

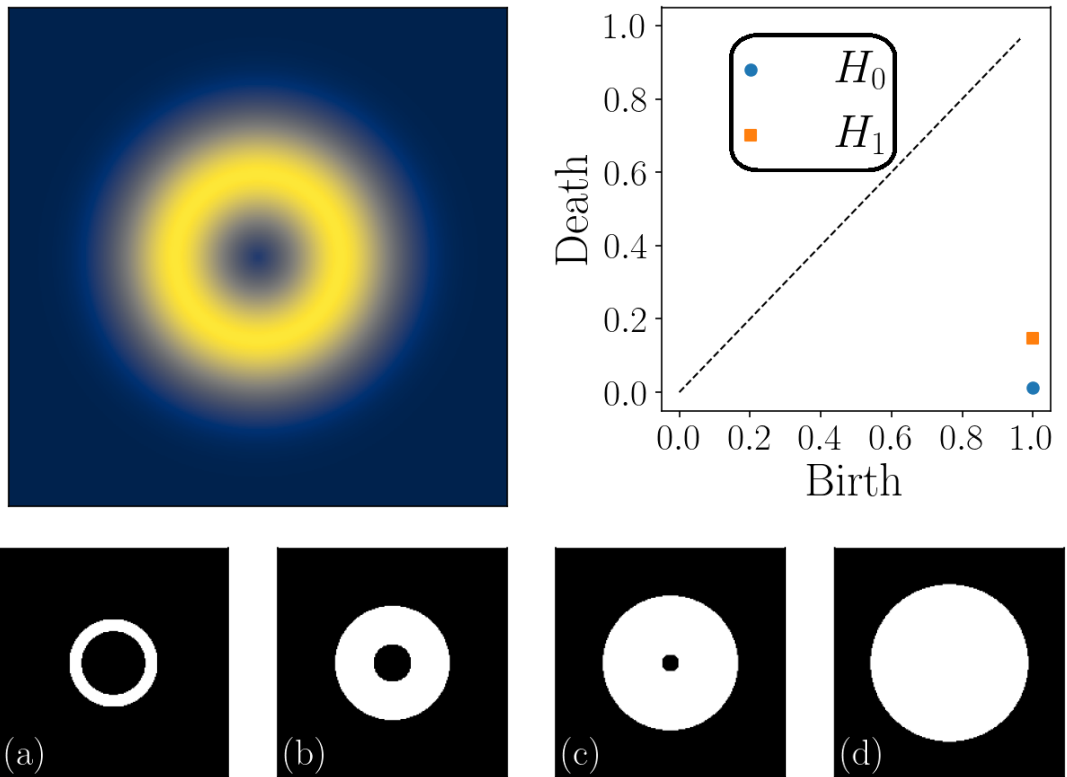


Figure 7: Illustration of superlevel-set persistence for an annular probability density. Panels (a–d) show the binary superlevel sets of the field at thresholds  $L = 0.95, 0.6, 0.3$  and  $0.1$ , respectively. At high thresholds, only the most intense region of the ring remains visible, corresponding to a single connected component and loop. As the filtration level decreases, the ring thickens and closes the loop.

## B Topology-Informed Kernel Density Estimation

We use the method in [21] to estimate the KDE in high dimensions. The method is summarised here.

### B.1 Kernel Density Estimation and Bandwidth Parameter

Given samples  $\{x_i\}_{i=1}^n \subset \mathbb{R}^d$ , the Gaussian kernel density estimate with bandwidth  $h > 0$  is

$$\hat{f}_h(x) = \frac{1}{nh^d} \sum_{i=1}^n \exp\left(-\frac{\|x - x_i\|^2}{2h^2}\right).$$

The bandwidth  $h$  governs the smoothness of the estimate: small  $h$  produces undersmoothing (spurious oscillations), while large  $h$  causes oversmoothing and loss of structure. Our objective is to select  $h$  through a purely unsupervised, topology-driven loss.

### B.2 Persistence Diagram and Topological Summary

For each bandwidth  $h$ , computing superlevel persistence yields a persistence diagram  $D_h$  containing all homological features across all thresholds  $L$ . For the purpose of bandwidth selection, we restrict attention to  $H_0$  (connected components) and measure:

- the *betti number*

$$\text{count}(h) = |D_h|,$$

- the *total persistence*

$$\text{TP}(h) = \sum_{(b,d) \in D_h} (b - d).$$

These quantities summarize how structured or oscillatory the KDE is at bandwidth  $h$ .

### B.3 Topology-Based Loss Function

The bandwidth is chosen by minimizing a loss composed only of these two terms:

$$\mathcal{L}(h) = \alpha_{\text{TP}} \text{TP}(h) + \alpha_{\text{count}} \text{count}(h),$$

where  $\alpha_{\text{TP}}$  and  $\alpha_{\text{count}}$  are fixed nonnegative weights (typically both set to 1 in our experiments). Larger bandwidths reduce both terms but oversmooth the density, eliminating meaningful peaks; smaller bandwidths inflate both terms by creating many spurious components. Thus, the loss is minimized at an intermediate, data-driven scale. Since  $\mathcal{L}(h)$  is one-dimensional, we optimize  $h$  using stochastic gradient descent. The gradient is obtained through differentiable KDE combined with a differentiable persistence pipeline.